ADVANCED MATERIALS
www.advmat.de

Coherent Precipitates with Strong Domain Wall Pinning in Alkaline Niobate Ferroelectrics

Changhao Zhao, Shuang Gao, Hans-Joachim Kleebe, Xiaoli Tan, Jurij Koruza, and Jürgen Rödel**

High-power piezoelectric applications are predicted to share approximately one-third of the lead-free piezoelectric ceramic market in 2024 with alkaline niobates as the primary competitor. To suppress self-heating in high-power devices due to mechanical loss when driven by large electric fields, piezoelectric hardening to restrict domain wall motion is required. In the present work, highly effective piezoelectric hardening via coherent plate-like precipitates in a model system of the (Li,Na)NbO_3 (LNN) solid solution delivers a reduction in losses, quantified as an electromechanical quality factor, by a factor of ten. Various thermal aging schemes are demonstrated to control the average size, number density, and location of the precipitates. The established properties are correlated with a detailed determination of short- and long-range atomic structure by X-ray diffraction and pair distribution function analysis, respectively, as well as microstructure determined by transmission electron microscopy. The impact of microstructure with precipitates on both small- and large-field properties is also established. These results pave the way to implement precipitate hardening in piezoelectric materials, analogous to precipitate hardening in metals, broadening their use cases in applications.

1. Introduction

Piezoelectric materials, distinguished by their multitude of applications such as high-accuracy actuators, sensors, and transformers, are widely utilized in the fields of communications, energy, medicine, etc.[1–5] Hardening in piezoelectric materials, which inhibits ferroelectric domain wall motions and therefore reduces mechanical loss, is a critical technique for applications near the resonance frequency.[6–8] For several decades, chemical doping has been extensively studied in ferroelectrics. Acceptor doping was found to introduce asymmetrically-distributed charged point defects, which pin the ferroelectric domain walls by an internal bias field.[9–11] However, the deterioration of the hardening effect at large electric fields, which arises from the highly mobile oxygen vacancies, limits the high-power applications.[12,13] With the increasing demand for high-power applications such as ultrasonic cleaning/welding, medical ultrasonic devices, surface acoustic wave devices, etc.,[14,15] seeking an alternative hardening method, which is stable at large electric fields is of great necessity and significance.

Piezoelectric hardening using a composite approach was validated experimentally in $Na_{1/2}Bi_{1/2}TiO_3$—$BaTiO_3$:ZnO (NBT—BT:ZnO) composites.[16] It was suggested that the hardening effect originated from a mechanical interaction between the secondary-phase particles and ferroelectric grains.[17] However, the secondary ZnO phase was located predominantly at grain boundaries, thus only domains in the vicinity of grain boundaries could be influenced. Inspired by metallurgy,[18] precipitation hardening, which aims at introducing secondary-phase particles into the interior of the ferroelectric grains to exert a more direct and stronger interaction with the domain walls, was recently proposed and validated in the model system $(Ba,Ca)TiO_3$.[19] These secondary-phase particles are expected to be highly stable in large electric fields.

Both orientation and shape of precipitates have a pronounced influence on the hardening effect in metals.[20,21] This effect on the precipitate—twin-boundary (TB) interaction was studied by molecular dynamics simulations.[22,23] It was predicted that a plate-like precipitate with a large aspect ratio has a stronger pinning effect than a spherical precipitate with the same volume. Moreover, the pinning effect from a plate-like precipitate is maximized when its long axis is parallel to the TB. Since a ferroelectric domain wall can be regarded as a TB, this orientation and shape effect should also play an important role in domain

C. Zhao, S. Gao, H.-J. Kleebe, J. Rödel
Department of Materials and Earth Sciences
Nonmetallic Inorganic Materials
Technical University of Darmstadt
Alarich-Weiss-Straße 2, 64287 Darmstadt, Germany
E-mail: zhao@ceramics.tu-darmstadt.de;
roedel@ceramics.tu-darmstadt.de

X. Tan
Department of Materials Science and Engineering
Iowa State University
Ames, IA 50011, USA

J. Koruza
Institute for Chemistry and Technology of Materials
Graz University of Technology
Stremayrgasse 9, Graz 8010, Austria

The ORCID identification number(s) for the author(s) of this article can be found under https://doi.org/10.1002/adma.202202379.

DOI: 10.1002/adma.202202379

wall pinning. Precipitation allows to introduce secondary-phase particles into the grain interior with a defined aspect ratio. For example, in the MgO-partially-stabilized zirconia (Mg-PSZ), coherent ellipsoidal precipitates with tetragonal symmetry (low-Zr content) were formed in a cubic matrix (high-Zr content).[24] In Fe-containing MgO, octahedral $FeMg_2O_4$ precipitates developed in the MgO matrix[25,26]

In addition, the morphology, size, distribution, and number density of the precipitates determine the final hardening effect. The formation of a secondary-phase particle can be divided into two regimes: nucleation (increase in number density) and growth (increase in size).[27] In a phase diagram where solubility decreases with decreasing temperature, low temperature is thermodynamically favored while high temperature is kinetically favored for both processes. Therefore, an optimal temperature regime exists for each process separately with the optimal temperature for precipitate nucleation lower than for precipitate growth.[27] Ideally, high number density with an appropriate average size (a few tens to hundreds of nanometers) should have the highest pinning effect on domain walls. Realizing this microstructure by devising optimum aging parameters is thus the key to precipitation hardening.

Alkaline niobates are an important family of lead-free functional materials, which are promising candidates to replace the commercial ferroelectric material $PbZr_{1-x}Ti_xO_3$ (PZT).[28] (K,Na)NbO_3-based (KNN) materials possess the largest market share of lead-free piezoelectric ceramics.[14] While high Q_m values (reciprocal of the mechanical loss, usually taken as part of the figure-of-merit for resonance applications[1]) were achieved in KNN-based materials by acceptor doping,[29,30] they suffer a drop at high vibration velocities which warrants improvement for high-power applications.[31,32] Considering the discussion above, it is highly attractive to precipitate plate-like secondary-phase particles in alkaline niobate solid solutions. A feasible alkali niobate is (Li,Na)NbO_3 (LNN), which was found to be promising for high-frequency applications such as frequency filters.[33,34] Although extensive studies were conducted on the electromechanical and dielectric properties, and the crystallographic structure of LNN,[35–37] there is no research investigating the secondary phase and its influence on the macroscopic properties in LNN. Belyaev et al. proposed an equilibrium phase diagram of LNN, indicating that the solid solubility of $LiNbO_3$ (LN) in the matrix $NaNbO_3$ (NN) drops from ≈30 mol% at 1000 °C to ≈12 mol% at 800 °C.[38] Such strong temperature dependence of solubility renders LNN an ideal system for precipitation hardening. In addition, the small-radius cations on the A-site retain sufficient atomic diffusivity at a relatively low temperature. This allows for optimized nucleation, while the precipitate growth rate is in a reasonable range.

Precipitation hardening was therefore designed in (Li,Na)NbO_3 (LNN) polycrystalline ceramics in this work. Both ferroelectric and electromechanical properties were investigated as a function of microstructure: precipitation-hardened samples have a strongly suppressed polarization and a greatly enhanced mechanical quality factor Q_m. Succinct results on the piezoelectric hardening effect were correlated to detailed studies on structure by X-ray diffraction, pair distribution function analysis, and transmission electron microscopy. The huge impact of precipitates on piezoelectric hardening provides a guide for wide implementation of this concept in KNN-based materials and beyond.

2. Experimental Section

2.1. Sample preparation

The phase diagram of LNN is presented in **Figure 1**.[38] The composition of $Li_{0.18}Na_{0.82}NbO_3$ (LNN18) was selected due to its moderate Li content and ferroelectricity at room temperature. Further increasing the Li content leads to a dramatic decrease in electromechanical and dielectric properties.[34] To study the effect of Li content on the properties of a single-phase sample before and after aging, single-phase samples with compositions of $Li_xNa_{1-x}NbO_3$ (x = 0.12, 0.14, and 0.16, denoted by LNN12, LNN14, and LNN16, respectively) were also prepared for reference. All samples were synthesized by the solid-state reaction method. Powders of Li_2CO_3 (99.0%, Alfa Aesar), Na_2CO_3 (99.5%, Alfa Aesar), and Nb_2O_5 (99.9%, Alfa Aesar) were weighed in a stoichiometric ratio. 1% excess of Na_2CO_3 was added into the mixture to compensate for volatilization during sintering. The mixture was ball-milled in a planetary mill at 250 r min^{-1} for 12 h with zirconia balls and ethanol as the media. The dried powders were then calcined at 850 °C for 4 h and resulted in a mixture of NN-rich solid solution (NN_{ss}, perovskite structure) and LN-rich solid solution (LN_{ss}, ilmenite structure), as confirmed by X-ray diffraction (XRD; Figure S1a, Supporting Information) since the calcination temperature of 850 °C lies within the two-phase region NN_{ss} + LN_{ss} (Figure 1).[38] The calcined powders were then cold isostatically pressed into pellets of a dimension of ≈Φ 10 mm × 1.5 mm with a pressure of 357 MPa. To obtain a single-phase sample and to avoid cracks, the samples were first sintered at 1300 °C for 2 h, followed by a moderate cooling at a rate of 5 K min^{-1}.

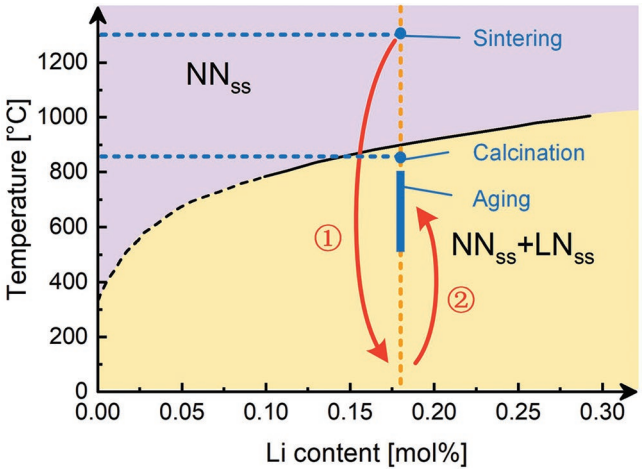

Figure 1. Partial phase diagram of the LNN solid solution (redrawn based on information in ref. [38]). The dashed part of the subsolidus curve was not determined. All heat treatments during precipitation are indicated by red arrows and the sequence is labeled with numbers (step ① is air quenching). The selected composition (gold dashed line), calcination/sintering temperature (blue dot), and aging temperature range (blue bar) are indicated in the phase diagram.

Then, specimens were thinned down to ≈0.5 mm to facilitate swift attainment of thermal equilibrium and reduce the possibility of crack formation.[39] These samples were heat-treated at 1300 °C for 2 h followed by air quenching. These as-quenched samples are hereafter denoted as unaged samples.

In the following, one-stage aging denotes samples aged at 500–800 °C for 8 h. Two-stage aging was also devised to nucleate the precipitates at the first stage (500 °C) for 24 h and grow them at the second stage (600 °C).[19] The duration of the second-stage aging varied from 0 h to 6 h. All aging was performed above the Curie temperature (≈480 °C, as determined from the permittivity curves in Figure S2, Supporting Information).

2.2. Structural Characterization

The XRD was conducted on powders, derived from crushed bulk sintered samples and annealed at 400 °C for 30 min to eliminate residual stress, using a laboratory X-ray diffractometer (Bruker D8 Advanced, Germany) with Cu Kα radiation (wavelengths $\lambda_{K\alpha1}$ = 1.5406 Å and $\lambda_{K\alpha2}$ = 1.5444 Å) and Bragg–Brentano geometry. Bright-field transmission electron microscopy (TEM), scanning TEM (STEM), and element mappings were conducted using a JEM-2100F transmission electron microscope (JEOL, Tokyo, Japan) with an Oxford X-Max80 energy-dispersive X-ray spectroscopy (EDS) detector (Oxford Instruments, High Wycombe, United Kingdom) attached to the instrument. A Φ 3 mm disk sample was cut and polished from ≈300 µm down to 20 µm in thickness. Annealing at 200 °C for 0.5 h with a heating and cooling rate of 1 K min^{-1} was carried out on the polished thin disk to release accumulated strain during polishing. The as-annealed disk was mounted on a molybdenum grid and subsequently, ion milled to electron transparency (Gatan model 600 dual ion mill).

Pair distribution functions (PDFs) were converted from the total scattering functions, which were obtained at the beamline P02.1 at Deutsches Elektronen-Synchrotron (DESY), with a wavelength of 0.2073 Å. Transmission mode was adopted. An area detector was used for data collection and the sample-to-detector distance was 200 mm. Each pattern was collected for 10 min to ensure a sufficient signal/noise ratio at high-Q range (Q is the amplitude of the transfer momentum). A background pattern was taken for 5 min with the same setup but without a sample. The conversion from a total scattering pattern to a PDF was conducted with PDFgetX3.[40] The simulation of PDF was performed with PDFgui.[41] For the two-phase model used in the PDF simulation, the $Pmc2_1$ model (NN_{ss}) was obtained by small-box modeling[42] based on the data of the unaged sample; the $R3c$ (LN_{ss}) was taken from the Inorganic Crystal Structure Database (ICSD No. 250775).

2.3. Electrical Measurements

The large-signal polarization hysteresis loop was monitored with a modified Sawyer–Tower circuit. Bar samples with a dimension of ≈5.5 mm × 1.5 mm × 0.3 mm were prepared and furnished with platinum electrodes on the two largest faces. The sample was immersed in silicone oil during the measurement. A triangular-wave electric field with a frequency of 1 Hz was adopted. The small-signal electromechanical properties were obtained through the impedance method. Before the electromechanical measurement, samples were poled under 8 kV mm^{-1} at 100–120 °C for 15 min. Disk samples with a dimension of ≈Φ 8 mm × 0.3 mm and radial vibration mode were adopted according to the European standard.[43] The impedance spectra were quantified by a commercial broadband impedance analyzer (Novocontrol, Montabaur, Germany). The amplitude of the applied AC electric field was 0.01 kV mm^{-1}. The mechanical quality factor Q_m was calculated with the 3 dB method. The longitudinal piezoelectric coefficient d_{33} was determined using a commercial Berlincourt meter (Piezotest PM300, Singapore), with a static clamping force of 2 N, a dynamic driving force of 0.25 N, and a driving frequency of 110 Hz. All the electromechanical parameters (i.e., Q_m, k_p, and d_{33}) were quantified on 3–4 samples, and the average values were taken. The error bars represent the standard deviation. Q_m at high vibration velocity was quantified by the burst method.[44] 2000 cycles of sinusoidal electric field at the resonance frequency were adopted to drive the sample. Then, the sample was short-circuited and the vibration starts to decay due to mechanical loss, based on which the electromechanical properties were determined. A laser vibrometer (OFV-505, Polytec GmbH, Waldbronn, Germany) was adopted to record the vibration of the sample throughout the whole process. The amplitude of the driving voltage was determined at the largest vibration velocity ≈0.8 m s^{-1}, which is the detection limit of the laser vibrometer. The details of the high-vibration-velocity Q_m measurement were described elsewhere.[45]

3. Results

3.1. Crystallographic Structure and Microstructure

3.1.1. Crystallographic Structure

The XRD patterns of the unaged and aged LNN18 samples are depicted in **Figure 2**a,b. In the unaged sample, only a single phase NN_{ss} with $R3c$ space group can be detected, verifying that the formation of the secondary phase was avoided by air quenching. After aging, a secondary phase appears, which is determined to be LN_{ss} also with space group $R3c$. Note that the LN_{ss} has a different structure type from the NN_{ss}, although they belong to the same space group. The three most intense reflections of the LN_{ss} phase are marked by asterisks. Due to the relatively small phase fraction of the LN_{ss} phase and small scattering factor of Li, the most intense reflection 012_{LN} (hexagonal coordinate system) was selected to evaluate the amount of LN_{ss} phase as a semi-quantitative method. The integrated intensity ratio of the 012_{LN} and the 100_{NN} reflections (reflection indexes of NN_{ss} are based on the pseudocubic coordinate system with the lattice constant of ≈4 Å) was taken as a measure for the amount ratio (denoted by w) of LN_{ss} and NN_{ss} phases (Figure 2c).

For one-stage aged samples, the amount of LN_{ss} phase increases with increasing aging temperature and reaches the maximum w value of 0.045 at 700 °C and then decreases to

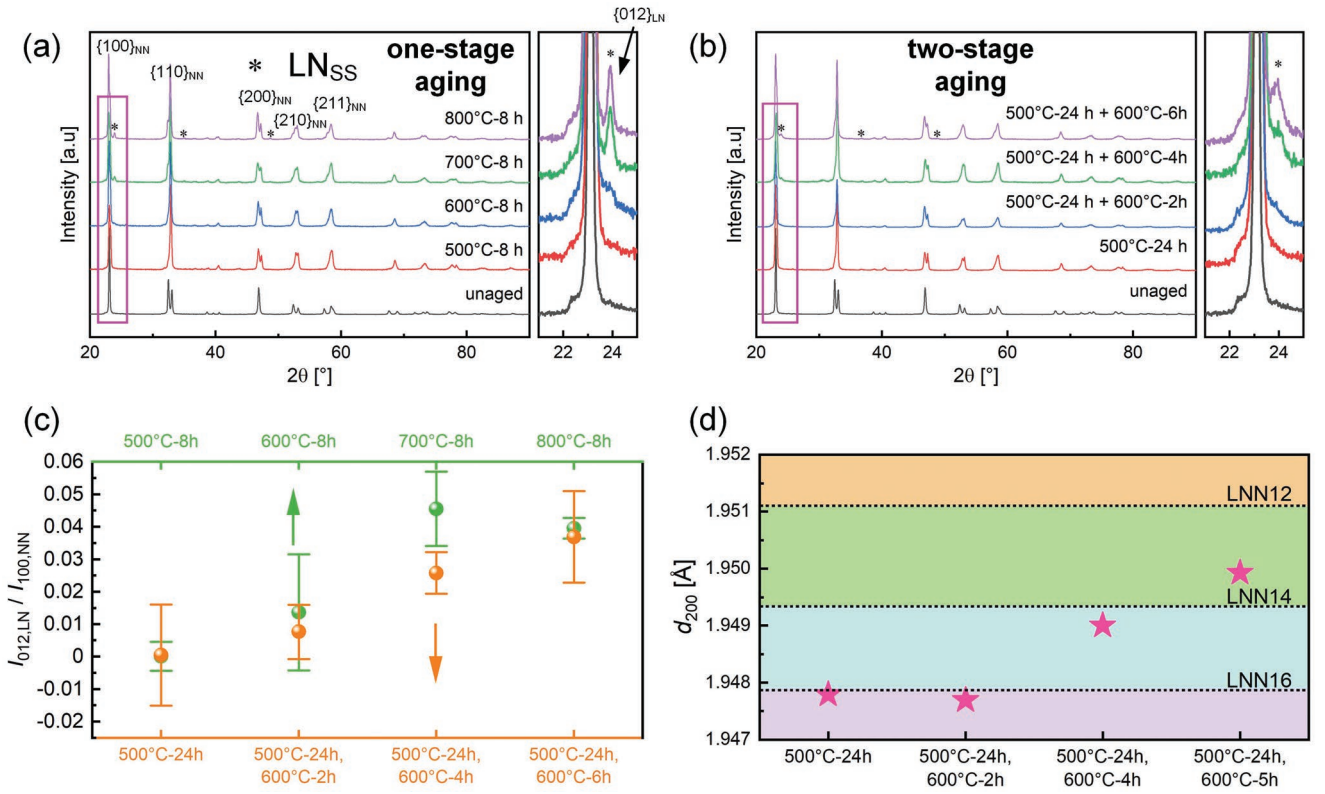

Figure 2. a,b) XRD patterns of unaged LNN18 and one-stage aged (a) and two-stage aged (b) LNN18. The positions of the three most intense reflections of the LN_{ss} phase are marked by asterisks. An enlarged plot of the 2θ range of 21°–25° is displayed in the right panel. c) The ratio of the integrated intensity of the 012_{LN} reflection, $I_{012,LN}$, and the $\{100\}_{NN}$ reflections, $I_{100,NN}$. d) The d-spacing of the $(200)_{NN}$ plane, d_{200}, of the two-stage aged samples. The d_{200} of unaged LNN12, LNN14, and LNN16 are indicated by the horizontal dashed lines.

0.039 at 800 °C. On the other hand, the amount of LN_{ss} phase increases with increasing duration of the second-stage aging with w up to 0.037. For one-stage aging, a higher aging temperature leads to a larger growth rate, but a smaller driving force for the precipitation since the difference between the solubility and overall solute concentration decreases. Therefore, an optimal aging temperature with the largest precipitate amount is expected.

The low precipitate growth rate at 500 °C is echoed in small 012_{LN} reflections after 8 h of aging. In some cases, it can take an impractically long time to grow the nuclei in the nucleation temperature regime, e.g., it takes 10 000 h to reach the peak aged condition in Mg-9 wt.%Al-1 wt.%Zn alloy.[46] On the other hand, aging at higher temperatures leads to a low number density of precipitates. This problem can be solved by multi-stage aging[47] or dynamic aging.[48] In the present study, two-stage aging was adopted. It is assumed that the nucleation process dominates the first stage at 500 °C, while the precipitate growth dominates the second stage at 600 °C. With the increasing duration of the second stage, the average size of the precipitates should increase, while the number density should remain unchanged. Hence, the amount of the LN_{ss} phase is effectively increased by extending the second-stage duration.

Besides the emergence of LN_{ss} reflections, there are other structural changes in the matrix NN_{ss} phase upon aging: both a splitting of the 200_{NN} can be observed and superlattice reflections in the 2θ range of ≈35–41° change, suggesting that the matrix NN_{ss} phase experiences a phase transition from rhombohedral ($R3c$) to orthorhombic ($Pmc2_1$). Peel et al. reported that there was a two-phase coexistence of $R3c$ and $Pmc2_1$ in LNN within the composition range of $0.08 \leq x \leq 0.20$, and the rhombohedral phase is favored by higher annealing temperature and rapid cooling.[49] Referring to the phase diagram, a higher annealing temperature aids in dissolving more Li while rapid cooling prevents the precipitation of LN_{ss} phase. Therefore, it can be inferred that the symmetry of the NN_{ss} phase depends on Li content. For further proof, the XRD patterns of as-quenched unaged LNN samples with different Li content ($0.12 \leq x \leq 0.18$) were compared (Figure S1b, Supporting Information). The gradual transition from $R3c$ to $Pmc2_1$ with decreasing Li content in the composition range of x = 0.12–0.18 confirms the compositional change prompts a phase transition in the NN_{ss} phase. Hence, the phase transition from $R3c$ to $Pmc2_1$ detected here is attributed to the reduction of the Li content in the NN_{ss} phase during the aging process.

The reflections from NN_{ss} shift to lower 2θ angles after aging, indicating a lattice expansion of the matrix. This is attributed to the substitution of Li-ions in the matrix with larger Na-ions. The observed trend of monotonically decreasing lattice parameter with increasing Li content in the unaged LNN (Figure S1b, Supporting Information) had also been reported before.[50] Therefore, a comparison of the lattice parameters of

the NN_{ss} phase provides an estimate of the matrix Li content in the aged samples. To this end, *d*-spacing of the $(200)_{NN}$ planes, d_{200}, for the two-stage aged samples was selected as an indicator for the change in lattice parameter change and calculated using Bragg's law. The d_{200} values of the two-stage aged samples are depicted in Figure 2d and contrasted to the d_{200} of unaged LNN12, LNN14, and LNN16 (LNN18 is not shown since it is rhombohedral-dominated, while the others are orthorhombic-dominated). Except for the d_{200} of the 500 °C-24 h + 600 °C-2 h sample, which is similar to that of the aged 500 °C-24 h sample, the d_{200} increases with increasing duration of the second-stage aging, indicating a decreasing Li content in the matrix due to precipitate growth.

3.1.2. Microstructures

Bright-field transmission electron microscope (TEM) images of LNN18 samples with different aging conditions are depicted in **Figure 3**a–e. The 600 °C-8 h sample (Figure 3a) has homogeneous plate-like intragranular precipitates with dimension of ≈290 nm × 30 nm (the dimension is determined from the edge-on viewed precipitates in the TEM images, representing the measured length of the long axis and short axis of the precipitates). There are also circular precipitates, which are believed to be platelets inclined to the viewing direction. Higher aging temperatures lead to larger precipitates (≈1800 nm × 140 nm for 700 °C-8 h sample, Figure S3a, Supporting Information), but their number density drops substantially. The 800 °C-8 h sample has almost no intragranular precipitates (Figure S3b, Supporting Information); instead, intergranular precipitates are observed (Figure 3b). This is consistent with the solid phase transition theory that lower aging temperature avails homogeneous nucleation inside grains.[27] Due to the lower nucleation energy barrier, lowering the aging temperature can decrease the difference between the nucleation energy barriers of grain boundary and grain interior and thus increase the fraction of nucleation inside grains. For the two-stage aged sample, dot-like features emerge in the sample after the first-stage aging (500 °C-24 h, Figure 3c). With the second-stage aging at 600 °C, the plate-like precipitates appear in the sample and the precipitates grow with increasing duration of second-stage aging (Figure 3d,e, with dimensions of ≈130 nm × 14 nm and ≈260 nm × 20 nm, respectively).

The energy-dispersive X-ray spectroscopy (EDS) map in Figure 3f demonstrates that the plate-like precipitates are Na-deficient, while Nb and O are homogeneously distributed in the matrix. This confirms that the precipitates are of LN_{ss} phase.

The small size of dot-like features in the 500 °C-aged sample (≈10 nm) makes their analysis by EDS or electron diffraction challenging. A plausible explanation is that these features are precursors at the premature stage of precipitates (resembling the so-called Guinier–Preston zones in metals,[27]), or dislocation loops,[51,52] both of which exhibit a pronounced TEM contrast due to internal strains. To determine this, a pair distribution function (PDF) analysis, as presented below, was performed to examine whether there are LN_{ss} precipitates forming at a short length scale after aging at 500 °C.

3.1.3. Pair Distribution Function Study of the Early Stage of Precipitation

PDF is a useful technique to study the local structure of materials, reflecting the relative position between all atom pairs in real space.[42,53] The high-*r* and low-*r* regions of the PDFs, which correspond to the short-range and intermediate-range structures of the unaged and 500 °C-8 h samples, are depicted in **Figure 4**a,b, respectively. In the high-*r* region, the PDF of the 500 °C-aged samples has a shift to the high-*r* direction, compared to the unaged sample. This indicates a lattice expansion of the NN_{ss} phase and is consistent with the long-range structural change observed from XRD. Changes in the peak shape in the high-*r* region of the PDF are attributed to the symmetry change from rhombohedral to orthorhombic after aging, as evidenced in the XRD study.

In the low-*r* region, the changes in PDF are less significant, indicating that the aged sample has a similar short-range structure as the unaged sample. Nevertheless, after aging at 500 °C, the atom-pair peaks at $r = 3.90$, 5.50, 6.71, 7.76, 8.67, and 9.49 Å, which arise from Nb—Nb atom pairs at different atom-pair distances, become lower in intensity. This can be attributed to an increase in atomic displacive disorder after aging, since the LN_{ss} phase, which has different Nb displacement from that in the NN_{ss} phase, is introduced at the local scale. In addition, new peaks at $r = 5.84$ and 8.20 Å arise after aging (indicated by red arrows). Since the size of the LN_{ss} at the early precipitation stage is only a few unit cells, the low-*r* region of PDF is sensitive to the emergence of the LN_{ss} phase. A series of low-*r* PDFs of a two-phase model consisting of the NN_{ss} phase ($Pmc2_1$) and the LN_{ss} phase ($R3c$) with different LN_{ss} fractions were simulated (Figure 4c). The simulated PDFs assign the peaks at $r = 5.84$ and 8.20 Å more prominence with increasing LN_{ss} phase fraction. The positions of these peaks are consistent with the newly emerged peaks in the experimental PDF of the 500 °C-8 h sample, highlighting that LN_{ss} forms very small precipitates upon aging at 500 °C.

3.2. Electrical Properties

3.2.1. Large-Signal Polarization Hysteresis Loops

Wake-Up Effect on the P–E Loop During Electric Field Cycling: A change in the shape of the *P–E* loop with electric field cycling was observed in all LNN samples and quantified in terms of maximum polarization. This so-called "wake-up" effect was also observed in other materials.[54–56] The unaged LNN18 is taken as an example and its *P–E* loops during cycling at 8 kV mm^{-1} are depicted for 400 cycles in **Figure 5**a and as a function of cycle number in Figure 5b. A gradual increase in maximum polarization P_m, remanent polarization P_r, and the slope near E_c are observed with increasing cycle number and higher maximum field. The changes in the *P–E* loops suggest that domain wall motion is gradually activated during cycling.

The "wake-up" effect was commonly observed in HfO_2-based and hard-doped PZT materials.[56] A widely accepted origin is the rearrangement of charged point defects. Due to the existence of oxygen vacancies (not only in acceptor-doped materials

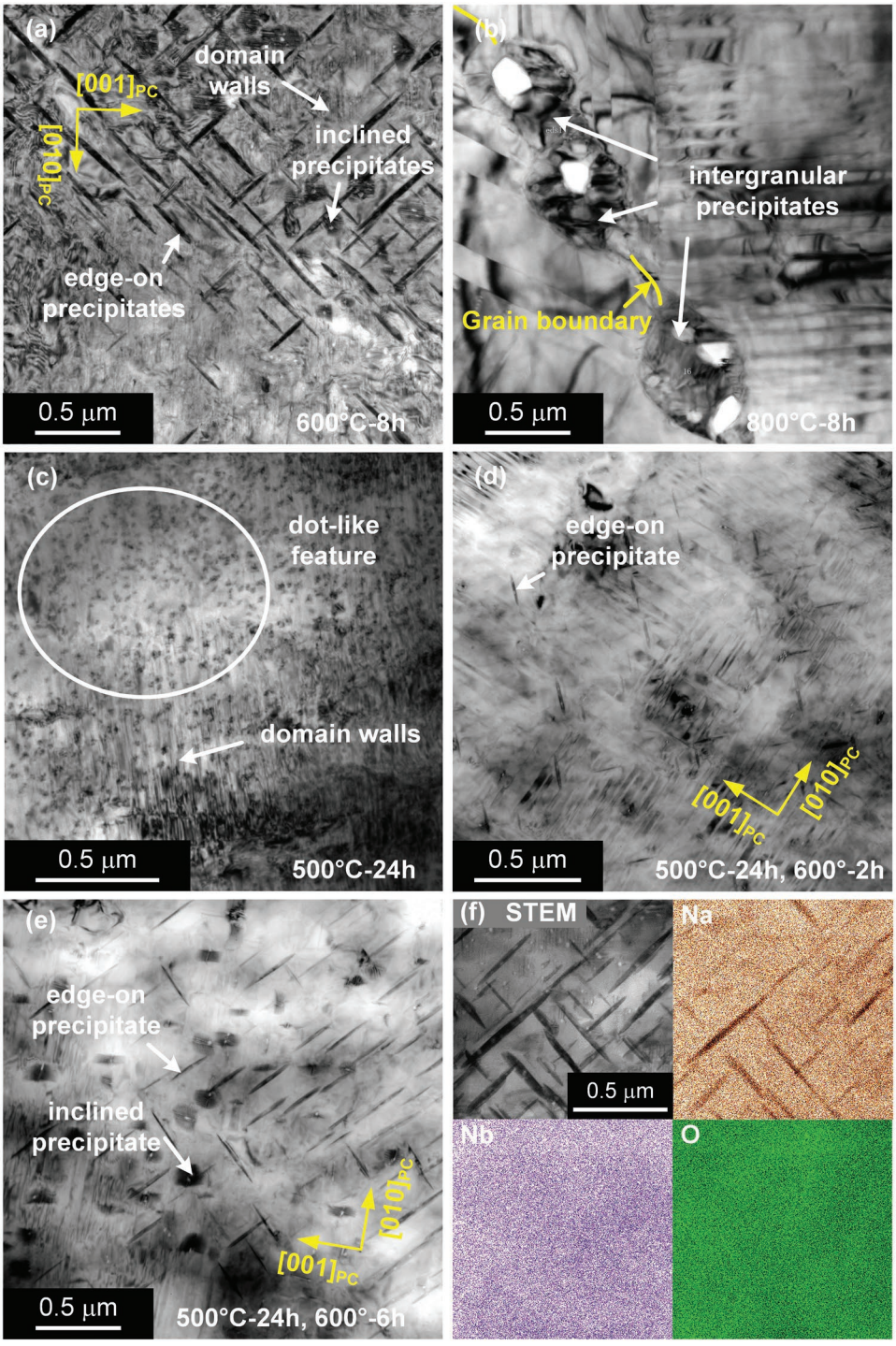

Figure 3. a–e) Bright-field TEM images of LNN18 samples aged at different conditions. f) The scanning TEM (STEM) image and EDS mapping of the 600 °C-8 h sample.

but generally in all ferroelectrics[57]), an internal bias field is established that suppresses polarization. During the cycling process, oxygen vacancies are rearranged and the internal field diminishes, leading to an increase in polarization. In the LNN samples, deviation from the nominal composition could occur due to volatilization of alkaline elements. Also, quenching from a high temperature can lead to an enhanced oxygen vacancy concentration. Therefore, the "wake-up" effect in the LNN samples is suggested to result from the rearrangement of oxygen vacancies.

The Effect of Precipitates on the P–E Loop: The *P–E* loops of the LNN18 samples aged at different conditions are featured in **Figure 6**. These loops are all obtained with the maximum field of 8 kV mm^{-1} using samples cycled until the loop was stable.

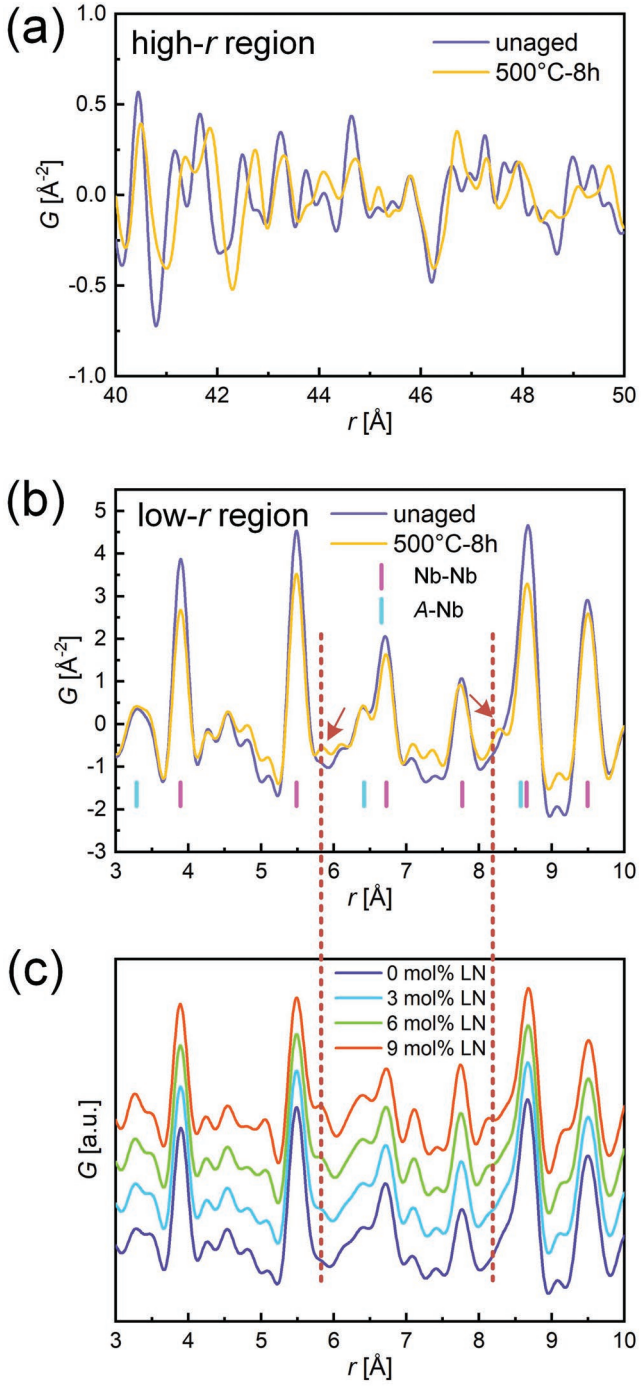

Figure 4. a) High-*r* region and b) low-*r* region of the atomic pair distribution functions (PDFs) of the unaged and 500 °C-8 h-aged LNN18. The origins of the major peaks in the low-*r* PDF are labeled by ticks with different colors. c) Simulated PDFs of the samples with coexistence of NN_{ss} phase and LN_{ss} phase.

The 500 °C- and 600 °C-aged samples (one-stage aging) have smaller P_m and more slanted loops, as compared to unaged samples (Figure 6a). Since the two samples have many intragranular precipitates, these precipitates can effectively pin domain walls and therefore reduce the polarization. On the other hand, the 700 °C-aged sample has a similar *P*–*E* loop to the unaged sample, and the 800 °C-aged sample has the highest P_m and a more square loop. This is attributed to the dominance of intergranular precipitates as compared to intragranular precipitates. Therefore, domain walls in the grain interior experience little pinning force from the precipitates.

Besides the domain wall pinning effect by the precipitates, the effect of compositional change in the matrix and precipitate/matrix interfaces is considered. The *P*–*E* loops of unaged LNN with Li content of 12–18 mol% indicate in Figure S4 (Supporting Information) that P_m increases with decreasing Li content in the selected compositional range (from 9.1 to 11.4 μC cm^{-2}). Note that aging leads to a decrease of Li content in the matrix which prompts an increase in P_m from the compositional effect. Therefore, the decrease in P_m after aging can be exclusively attributed to the precipitate effect. In addition, the significant enhancement in the polarization of the 800 °C-aged samples can be also attributed to: i) the Maxwell-Wagner effect arising from the introduction of precipitate/matrix interfaces,[58] and to ii) oxygen compensation during the aging at a proper temperature,[59] which weakens the domain wall pinning from the oxygen vacancies resulting from the quenching process.

For the two-stage aged samples (Figure 6b), the maximum polarization decreases with increasing aging duration of the second-stage aging. In addition, the loop of samples with a longer duration at the second aging stage is closer to a linear dielectric, which indicates that the domain walls in these samples are less active. Note that all samples were cycled at 8 kV mm^{-1}, but the "wake-up" effect barely occurs in the samples which underwent a long second-stage duration. In these samples, the domain walls are pinned not only by the point defects but also by the precipitates. Even though the point defects can be rearranged by the cycling, the domain walls are difficult to be depinned from the precipitates. The pinning force is stronger in the sample with precipitates of larger size (longer aging duration) and therefore the domain walls are more difficult to be activated. Note that in the one-stage aged samples (700 °C-8 h and 800 °C-8 h), the precipitates are also large in size, but the loops still feature the "wake-up" effect since there is a limited number density of the intragranular precipitates, while these prevail in the two-stage aged samples exerting strong pinning force.

3.2.2. Electromechanical Properties

The small-signal electromechanical parameters: mechanical quality factor Q_m, planar electromechanical coupling factor k_p, and piezoelectric coefficient d_{33}, are depicted in **Figure 7**a,b (the complete figures of merit for different types of applications are depicted in Figure S5, Supporting Information). An immense increase in Q_m from the unaged sample with a value of 80 to a value of 529 for aging for 8 h at 600 °C is striking, while little change in d_{33}, but lower k_p values (from 0.24 to 0.14) are noted. Compared to the 600 °C-8 h sample, samples aged at 500, 700, and 800 °C have lower Q_m and higher d_{33} and k_p, indicating that 600 °C is the optimal temperature for piezoelectric hardening for one-stage aging. This can be explained as such: for a low aging temperature (e.g., 500 °C), the number

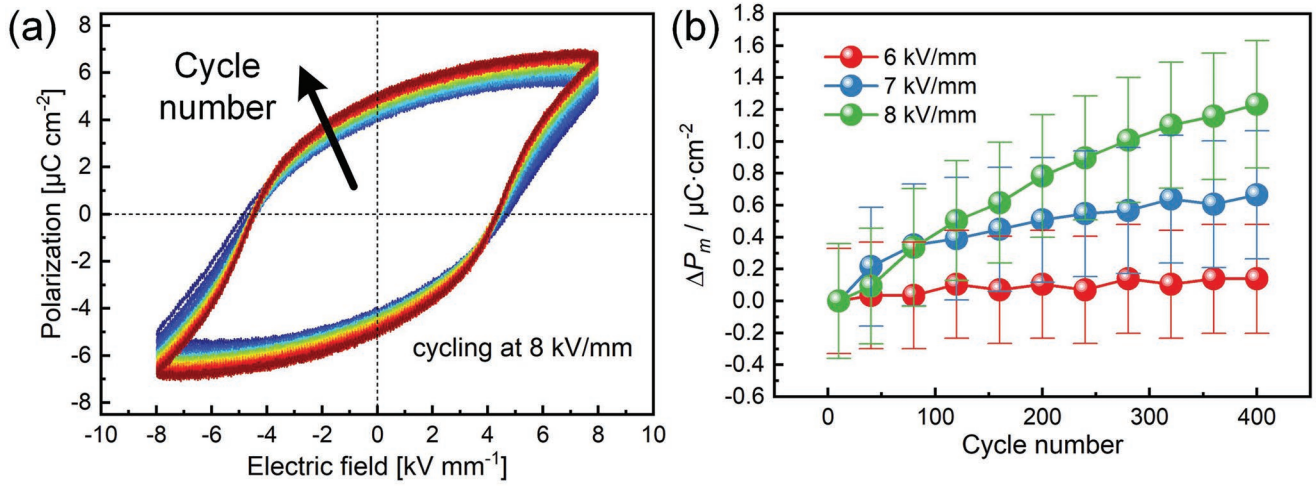

Figure 5. a) Evolution of the *P–E* loops of unaged LNN18 during electric field cycling at 8 kV mm^{-1} with a frequency of 1 Hz. The colors from blue to red represent the increasing cycle number. b) The increase in maximum polarization ΔP_m as a function of cycle number for different electric fields.

density of precipitates can be high but the size is too small to provide effective pinning on domain walls; while for a high aging temperature (e.g., 700 and 800 °C), the samples have fewer intragranular precipitates, thus there are only a small fraction of domain walls, which can be pinned by the precipitates. Specifically, the small-signal properties of the 800 °C-aged sample, which is almost free of intragranular precipitates, are comparable to those of the unaged sample. For the two-stage aged samples, the Q_m reveals values between ≈450–600 and features a decrease with increasing aging duration, together with d_{33} and k_p (Figure 6b). The duration of the second-stage aging mainly affects the precipitate size. The samples with larger precipitates have lower k_p and d_{33}. This can be explained as follows: The domain walls in the sample with larger precipitates are subjected to a stronger pinning force from the precipitates, resulting in a lower poling degree. Compared to the unaged sample, one-stage aging at a proper temperature range (500–700 °C) and two-stage aging can largely enhance the Q_m, also accompanied by a decrease in k_p and slightly enhanced d_{33}.

It is worth discussing whether the change in the electromechanical properties is due to the compositional change in the matrix or the precipitates. The Li content in the matrix of the 500 °C-24 h sample is close to that of unaged LNN16 according to Figure 2d. Compared to LNN16 (Q_m = 81, k_p = 0.25, d_{33} = 35.2), the 500 °C-24 h LNN18 features a tremendous enhancement in Q_m and decrease in k_p. This comparison demonstrates that precipitation far outweighs the attendant change in matrix composition.

To conclude the data analysis, we present strong proof of application relevance of precipitation hardening for high-power applications. For high-power applications, devices are working under large electric field excitation resulting in very high vibration velocities of up to 1 m s^{-1}. A large Q_m at high vibration velocities is essential for reducing the temperature rise in high-power applications. Figure 7c depicts the normalized Q_m of aged LNN18 as a function of vibration velocity in contrast to hard-doped PZT,[45] Mn-doped $KNbO_3$,[32] and Cu-doped KNN[31] (the absolute Q_m values of these materials as a function of

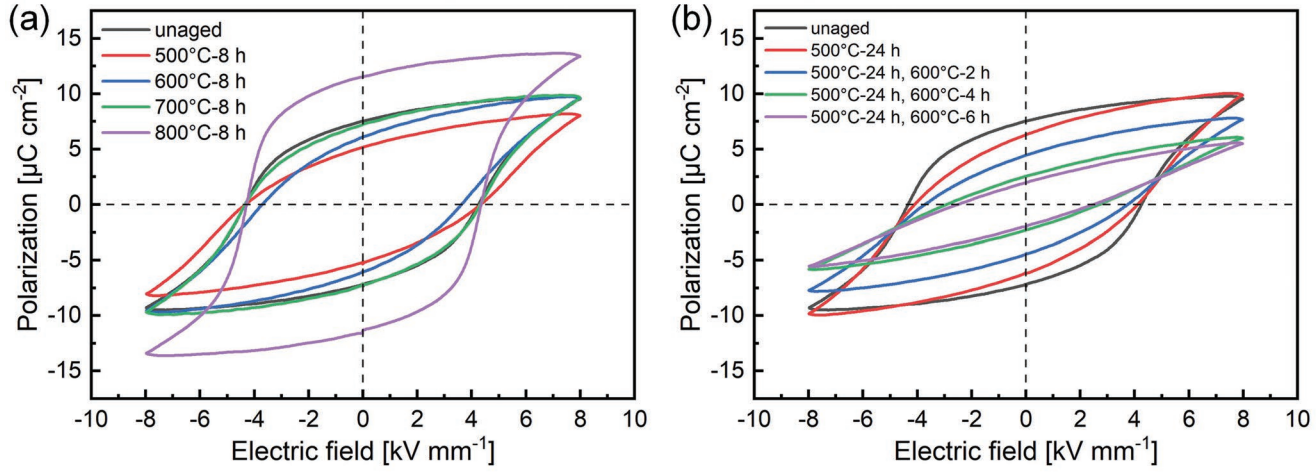

Figure 6. a,b) *P–E* loops of one-stage aged (a) and two-stage aged (b) LNN18 samples.

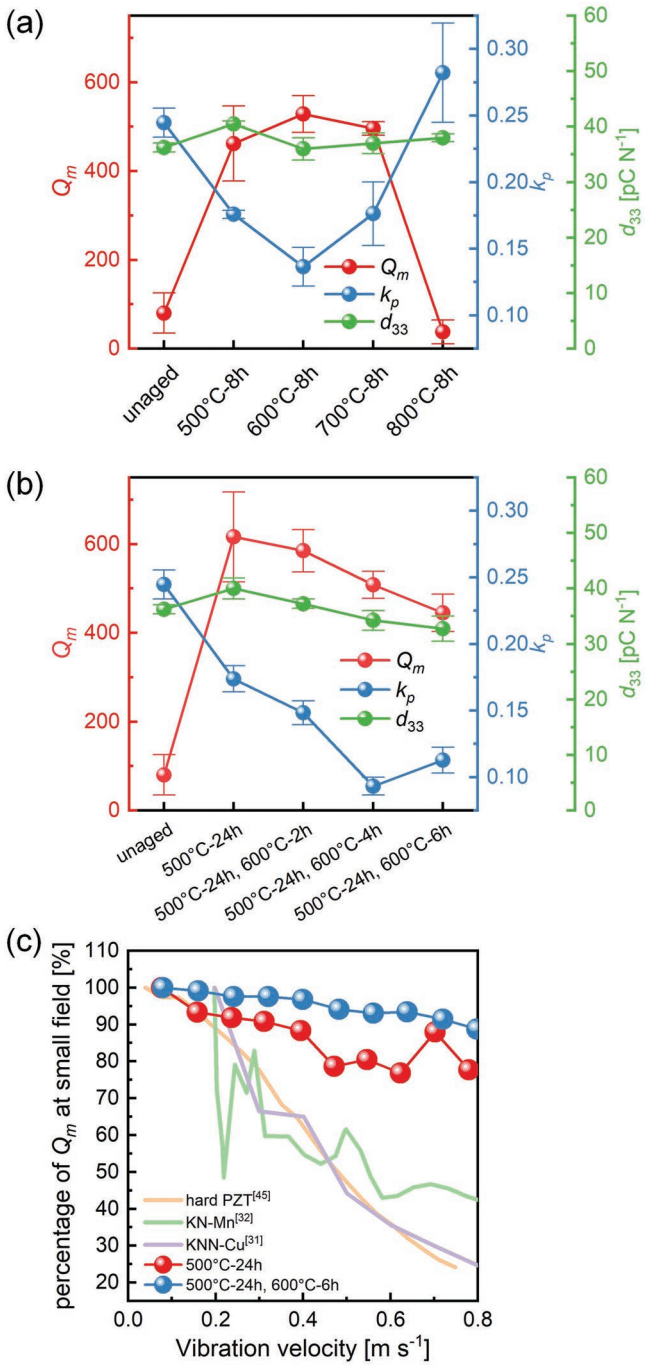

Figure 7. a,b) Mechanical quality factor Q_m, planar electromechanical coupling factor k_p, and piezoelectric coefficient d_{33} of one-stage aged (a) and two-stage aged (b) LNN18 samples. c) High-vibration-velocity property of aged LNN18, hard-doped PZT,[45] Mn-doped $KNbO_3$,[32] and Cu-doped KNN:[31] percentage of the small-signal Q_m as a function of vibration velocity.

vibration velocity can be found in Figure S6, Supporting Information). All the aged LNN18 samples have a stable Q_m up to a vibration velocity of ≈0.8 m s^{-1}. Specifically, the 500 °C-24 h sample and the 500 °C-24 h + 600 °C-6 h sample preserve 78% and 89% of their small-signal Q_m, respectively, at a vibration velocity ≈0.8 m s^{-1}, while the Q_m of other comparing materials drops to 20–40% of their small-signal Q_m value. The good stability of the Q_m in LNN18 indicates that the pinning effect from precipitates is persistent in high driving fields, providing a promising technique for high-power applications.

4. Discussion

The TEM results indicate that for one-stage aged samples, the aging temperature affects the number density, location, and size of the precipitates, while for two-stage aged samples, the duration of the second step determines the size of the precipitates. A relationship between precipitate morphology and macroscopic properties of the samples has been identified. For the one-stage aged samples, lower aging temperature leads to smaller remanent and maximum polarization and higher Q_m (Figures 6a and 7a), indicating that: I) the number of intragranular precipitates dominates the properties and II) the number of intragranular precipitates controls domain wall pinning. In **Figure 8**a, the P_r and Q_m were plotted as a function of the intensity ratio of the 012_{LN} reflection and $\{100\}_{NN}$ reflections for the two-stage aged samples, which is proportional to the relative amount of the LN_{ss} phase. As the second-stage aging tunes precipitate size, the larger intensity ratio indicates a larger precipitate size. It can be seen from Figure 8a that the P_r (assuming the compositional effect is negligible, as discussed in Section 3, and P_r reflects the pinning force of domain walls at large fields) is strongly dependent on precipitate size, while Q_m (which reflects the domain wall mobility at the small field) is much less dependent.

A schematic illustration of the precipitate size effect on the pinning effect is illustrated in Figure 8b. The increase in the length of the plate-like precipitate in metals can substantially increase the pinning force on the TBs.[22] A similar effect can be expected on the domain wall pinning effect from the precipitates. At low electric fields, both small precipitate and large precipitate effectively pin the domain walls, and therefore the small-signal Q_m is less dependent on precipitate size. At high electric fields, the small precipitate can be depinned by the large driving force, while the large precipitate can still pin the domain walls. Thus, the P_r is strongly suppressed in the sample with large precipitates.

In addition, it can be learned that the pinning effect on domain walls from intragranular precipitates differs significantly from that of intergranular precipitates. In the 800 °C-8 h sample, where most precipitates are located at grain boundaries, the electromechanical properties are barely affected (Figure 7a), and its large-signal polarization even has an enhancement compared to the unaged sample. All of these results indicate that intergranular precipitates in LNN cannot effectively pin the domain walls. Nevertheless, secondary-phase particles at grain boundaries were evidenced to be able to harden piezoelectric ceramics, e.g., ZnO inclusions in NBT-6BT.[16] The hardening effect of the NBT-6BT:ZnO composites was attributed to the field-induced strain incompatibility between the ferroelectric matrix NBT-6BT and non-ferroelectric inclusions ZnO. The extremely small field-induced strain in ZnO can provide internal stress which holds back the elongation of NBT-6BT in

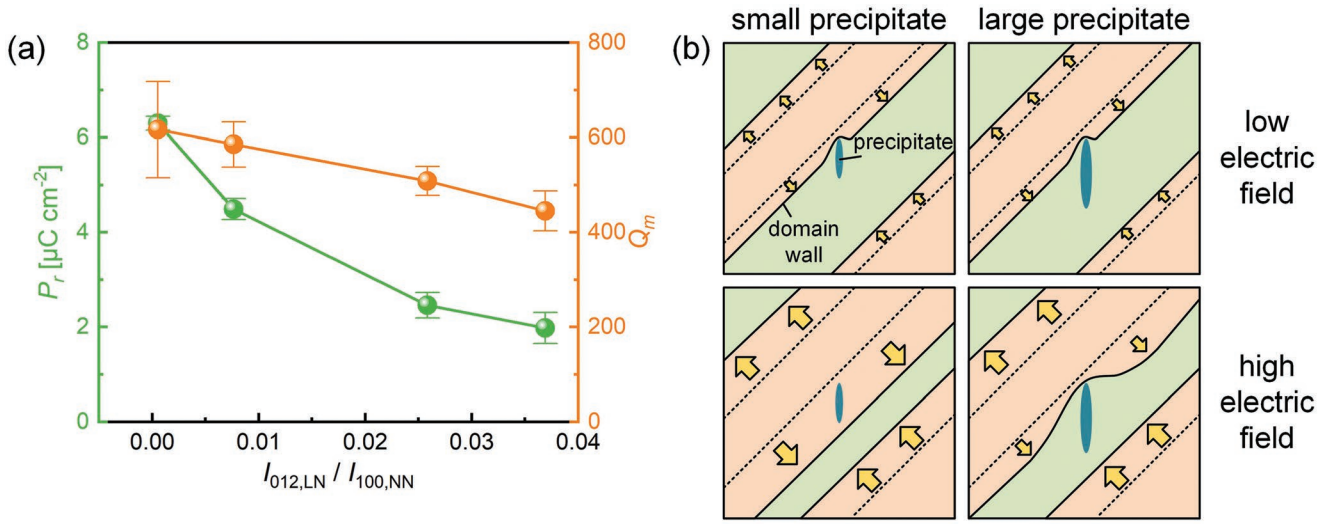

Figure 8. a) Remanent polarization P_r and mechanical quality factor Q_m of two-stage aged samples as a function of the intensity ratio of the 012_{LN} reflection and $\{100\}_{NN}$ reflections. b) Schematic of the precipitate size effect on the domain wall pinning under low and high electric field.

the field direction, therefore reducing domain wall contributions in NBT-6BT. Note that in our case, the precipitate LN_{ss} is ferroelectric. The difference in the field-induced strain between NN_{ss} and LN_{ss} is expected to be much smaller than that between NBT-6BT and ZnO, thus the incompatibility strain does not suffice to suppress the domain wall motion.

On the other hand, the intragranular precipitates interact with domain walls in a different way. According to a theoretical calculation in metals, when a TB tends to pass by a precipitate, the precipitate rotates elastically for a small angle, and the shear stress near the precipitate/matrix interface imposes a strong back-stress to the TB.[22] A similar effect is expected for a ferroelectric domain wall passing by a precipitate. Note that the pinning force on the domain wall is not related to the field-induced strain incompatibility of precipitate and matrix, but rather to the largest magnitude of the shear stress during the interaction process between the domain wall and the precipitate, which is dependent on the size, shape, and orientation of the precipitate. The suppressed large-signal polarization and substantially enhanced Q_m in the samples with a large number of intragranular precipitates prove that these coherent precipitates are much more effective at pinning domain walls compared to samples with intergranular precipitates.

The precipitation piezoelectric hardening demonstrated here can be implemented in other compositions, especially lead-free ones. The key requirement is the presence of a temperature-dependent solubility in the phase diagram, which is not uncommon. For example, in addition to the present $NaNbO_3$–$LiNbO_3$ binary system, such a feature has been reported in $LiNbO_3$–MgO,[60] $BaTiO_3$–$CaTiO_3$,[19,61] and $BaTiO_3$–Nd_2O_3.[62] Thermodynamic calculations can be conducted to identify additional systems with an inclined solvus line in phase diagrams with high-performing piezoelectric compositions as the solvent. It is noted that the design and development of piezoelectric ceramics has been centered on single-phase compositions in the past and those that exceed the solubility limit were rejected previously.[63,64] With the precipitate-hardening strategy demonstrated in the present work, many piezoelectric solid solutions should be revisited with quenching–aging thermal processing to enhance their properties. The KNN-based compositions are of particular interest because of their commercial potential and their close chemical similarity to the LNN compositions. By optimizing the aging conditions, $LiNbO_3$-rich coherent precipitates are expected to form in the interior of (K,Na,Li)NbO_3 grains and a significantly improved quality factor Q_m can be realized.

5. Conclusions

This work has successfully demonstrated piezoelectric hardening in the LNN18 ceramics, as representatives of alkaline niobate lead-free ceramics, through second-phase precipitation. Aging schemes are established to control the shape, size, number density and location of the precipitates, and coherent plate-like precipitates with optimized sizes are introduced in the LNN18 ceramics. The precipitates are observed to have a profound impact on the ferroelectric and electromechanical properties of the ceramics:

a) The large-signal polarization is suppressed in the LNN18 ceramics with intragranular precipitates of a high number density. The larger the size of the intragranular precipitates, the smaller the polarization due to the stronger pinning effect of the precipitates.
b) The weak-field mechanical quality factor, Q_m, exhibits one order of magnitude increase from ≈80 to ≈600 when coherent intragranular precipitates are introduced into the LNN18 ceramics. The enhanced Q_m can retain 89% of its value even at a vibration velocity of ≈0.8 m s^{-1}.

Supporting Information

Supporting Information is available from the Wiley Online Library or from the author.

Acknowledgements

The authors are indebted to the Deutsche Forschungsgemeinschaft (DFG) for funding under project number 462460745. X.T. acknowledges financial support form the U.S. National Science Foundation (NSF) through Grant No. DMR-2110264. The authors acknowledge DESY (Hamburg, Germany), a member of the Helmholtz Association HGF, for the provision of experimental facilities. Parts of this research were carried out at PETRA III and the authors would like to thank Alexander Schökel for assistance in using the beamline P02.1. Beamtime was allocated for proposal I-20210563.

Open access funding enabled and organized by Projekt DEAL.

Conflict of Interest

The authors declare no conflict of interest.

Data Availability Statement

The data that support the findings of this study are available from the corresponding author upon reasonable request.

Keywords

electromechanical hardening, high-power properties, mechanical quality factor, niobates, precipitation

Received: March 15, 2022
Revised: June 21, 2022
Published online: August 23, 2022

[1] K. Uchino, *Ferroelectric Devices*, CRC Press/Taylor & Francis Group, Boca Raton, FL, USA **2010**.
[2] J. Rödel, K. G. Webber, R. Dittmer, W. Jo, M. Kimura, D. Damjanovic, *J. Eur. Ceram. Soc.* **2015**, *35*, 1659.
[3] C. Qiu, B. Wang, N. Zhang, S. Zhang, J. Liu, D. Walker, Y. Wang, H. Tian, T. R. Shrout, Z. Xu, L. Chen, F. Li, *Nature* **2020**, *577*, 350.
[4] M. Mirhosseini, A. Sipahigil, M. Kalaee, O. Painter, *Nature* **2020**, *588*, 599.
[5] K. Park, C. K. Jeong, N. K. Kim, K. J. Lee, *Nano Convergence* **2016**, *3*, 12.
[6] K. Uchino, in *Advanced Piezoelectric Materials*, 2nd Ed., Woodhead Publishing, Cambridge, UK **2017**, Ch. 17.
[7] G. Liu, S. Zhang, W. Jiang, W. Cao, *Mater. Sci. Eng. R* **2015**, *89*, 1.
[8] K. H. Härdtl, *Ceram. Int.* **1982**, *8*, 121.
[9] X. Ren, *Nat. Mater.* **2004**, *3*, 91.
[10] G. H. Jonker, *J. Am. Ceram. Soc.* **1972**, *55*, 57.
[11] M. I. Morozov, D. Damjanovic, *J. Appl. Phys.* **2010**, *107*, 034106.
[12] M. Hejazi, E. Taghaddos, E. Gurdal, K. Uchino, A. Safari, *J. Am. Ceram. Soc.* **2014**, *97*, 3192.
[13] K. Uchino, J. H. Zheng, Y. H. Chen, X. H. Du, J. Ryu, Y. Gao, S. Ural, S. Priya, S. Hirose, *J. Mater. Sci.* **2006**, *41*, 217.
[14] M. Gagliardi, *Lead-Free Piezoelectric Ceramics: Technologies and Global Opportunities*, BCC Publishing, Boston, MA, USA **2019**.
[15] Y. H. Jung, S. K. Hong, H. S. Wang, J. H. Han, T. X. Pham, H. Park, J. Kim, S. Kang, C. D. Yoo, K. J. Lee, *Adv. Mater.* **2020**, *32*, 1904020.
[16] L. K. Venkataraman, L. M. Riemer, J. Koruza, J. Rödel, *Appl. Phys. Lett.* **2017**, *111*, 22905.
[17] L. K. Venkataraman, M. Hinterstein, K. Lee, T. Yang, L. Chen, P. B. Groszewicz, J. Koruza, J. Rödel, *Phys. Rev. B* **2020**, *101*, 174108.
[18] A. J. Ardell, *Metall. Trans. A* **1985**, *16*, 2131.
[19] C. Zhao, S. Gao, T. Yang, M. Scherer, J. Schultheiß, D. Meier, X. Tan, H. J. Kleebe, L. Q. Chen, J. Koruza, J. Rödel, *Adv. Mater.* **2021**, *33*, 2102421.
[20] L. Y. Wei, G. L. Dunlop, H. Westengen, *Metall. Mater. Trans. A* **1995**, *26*, 1705.
[21] J. F. Nie, *Scr. Mater.* **2003**, *48*, 1009.
[22] H. Fan, Y. Zhu, J. A. El-Awady, D. Raabe, *Int. J. Plast.* **2018**, *106*, 186.
[23] H. Fan, Y. Zhu, Q. Wang, *Comput. Mater. Sci.* **2018**, *155*, 378.
[24] D. L. Porter, A. H. Heuer, *J. Am. Ceram. Soc.* **1977**, *60*, 183.
[25] B. Reppich, H. Knoch, in *Deformation of Ceramic Materials*, (Eds: R. C. Bradt, R. E. Tressler), Springer, Boston. MA, USA **1975**.
[26] L. Gurnani, M. K. Singh, P. Bhargava, A. Mukhopadhyay, *Philos. Mag. Lett.* **2015**, *95*, 285.
[27] D. A. Porter, K. E. Easterling, M. Y. Sherif, *Phase Transformations in Metals and Alloys*, CRC Press, Boca Raton, FL, USA **2009**.
[28] K. Wang, B. Malič, J. Wu, *MRS Bull.* **2018**, *43*, 607.
[29] H. Han, J. Koruza, E. A. Patterson, J. Schultheiss, E. Erdem, W. Jo, J. Lee, J. Rödel, *J. Eur. Ceram. Soc.* **2017**, *37*, 2083.
[30] T. N. Nguyen, H. C. Thong, Z. X. Zhu, J. K. Nie, Y. X. Liu, Z. Xu, P. S. Soon, W. Gong, K. Wang, *J. Mater. Res.* **2021**, *36*, 996.
[31] E. A. Gurdal, S. O. Ural, H. Y. Park, S. Nahm, K. Uchino, *Sens. Actuators, A* **2013**, *200*, 44.
[32] H. Nagata, T. Takenaka, *Electron. Commun. Jpn.* **2013**, *96*, 53.
[33] R. R. Zeyfang, R. M. Henson, W. J. Maier, *J. Appl. Phys.* **1977**, *48*, 3014.
[34] R. M. Henson, R. R. Zeyfang, K. V. Kiehl, *J. Am. Ceram. Soc.* **1977**, *60*, 15.
[35] W. Śmiga, B. Garbarz-Glos, W. Piekarczyk, H. Noga, D. Sitko, M. Karpierz, M. Livinsh, *Integr. Ferroelectr.* **2016**, *173*, 46.
[36] G. R. Li, Q. R. Yin, L. Y. Zheng, Y. Y. Guo, W. W. Cao, *J. Electroceram.* **2008**, *21*, 323.
[37] C. Kus, M. J. Dambekalne, I. V. Brante, K. J. Borman Is, A. V. Plaude, *Ferroelectrics* **1988**, *81*, 281.
[38] I. N. Belyaev, V. B. Nalbandyan, Y. A. Ivanov, *Izv. Akad. Nauk SSSR, Neorg. Mater.* **1984**, *20*, 491.
[39] M. Zhang, P. Breckner, T. Frömling, J. Rödel, L. K. Venkataraman, *Appl. Phys. Lett.* **2020**, *116*, 262902.
[40] P. Juhás, T. Davis, C. L. Farrow, S. J. L. Billinge, *J. Appl. Crystallogr.* **2013**, *46*, 560.
[41] C. L. Farrow, P. Juhas, J. W. Liu, D. Bryndin, E. S. Bozin, J. Bloch, T. Proffen, S. J. Billinge, *J. Phys.: Condens. Matter* **2007**, *19*, 335219.
[42] D. Hou, C. Zhao, A. R. Paterson, S. Li, J. L. Jones, *J. Eur. Ceram. Soc.* **2018**, *38*, 971.
[43] European Committe for Electrotechnical Standardization, European Standard on Piezoelectricity: Part 2, EN 50324-2:2002, **2002**.
[44] M. Umeda, K. Nakamura, S. Ueha, *Jpn. J. Appl. Phys.* **1998**, *37*, 5322.
[45] M. Slabki, J. Wu, M. Weber, P. Breckner, D. Isaia, K. Nakamura, J. Koruza, *J. Am. Ceram. Soc.* **2019**, *102*, 6008.
[46] S. Celotto, *Acta Mater.* **2000**, *48*, 1775.
[47] W. F. Smith, N. J. Grant, *Metall. Trans.* **1970**, *1*, 979.
[48] X. L. Ma, S. E. Prameela, P. Yi, M. Fernandez, N. M. Krywopusk, L. J. Kecskes, T. Sano, M. L. Falk, T. P. Weihs, *Acta Mater.* **2019**, *172*, 185.
[49] M. D. Peel, S. E. Ashbrook, P. Lightfoot, *Inorg. Chem.* **2013**, *52*, 8872.
[50] I. Pozdnyakova, A. Navrotsky, *J. Am. Ceram. Soc.* **2002**, *85*, 379.
[51] J. Buha, R. N. Lumley, A. G. Crosky, K. Hono, *Acta Mater.* **2007**, *55*, 3015.
[52] T. Suzuki, M. Ueno, Y. Nishi, M. Fujimoto, *J. Am. Ceram. Soc.* **2001**, *84*, 200.
[53] T. Egami, S. J. L. Billinge, *Underneath the Bragg Peaks: Structural Analysis of Complex Materials*, Elsevier, Oxford, UK **2012**.
[54] T. Lu, Y. Tian, A. Studer, Q. Li, R. L. Withers, L. Jin, D. Yu, Z. Xu, X. Wei, Y. Liu, *Chem. Mater.* **2020**, *32*, 6456.

[55] Q. Zhang, W. Cai, C. Zhou, R. Xu, S. Zhang, Z. Li, R. Gao, C. Fu, *Appl. Phys. A* **2019**, *125*, 759.
[56] F. P. G. Fengler, M. Pešić, S. Starschich, T. Schneller, C. Künneth, U. Böttger, H. Mulaosmanovic, T. Schenk, M. H. Park, R. Nigon, P. Muralt, T. Mikolajick, U. Schroeder, *Adv. Electron. Mater.* **2017**, *3*, 1600505.
[57] K. Carl, K. H. Härdtl, *Ferroelectrics* **1977**, *17*, 473.
[58] P. Lunkenheimer, V. Bobnar, A. V. Pronin, A. I. Ritus, A. A. Volkov, A. Loidl, *Phys. Rev. B* **2002**, *66*, 052105.
[59] F. D. Morrison, D. C. Sinclair, A. R. West, *J. Am. Ceram. Soc.* **2001**, *84*, 531.
[60] M. Ferriol, A. Dakki, M. T. Cohen-Adad, G. Foulon, A. Brenier, G. Boulon, *J. Cryst. Growth* **1977**, *178*, 529.
[61] R. C. DeVries, R. Roy, *J. Am. Ceram. Soc.* **1955**, *38*, 142.
[62] N. Hirose, J. M. S. Skakle, A. R. West, *J. Electroceram.* **1999**, *3*, 233.
[63] Y. Guo, K. Kakimoto, H. Ohsato, *Appl. Phys. Lett.* **2004**, *85*, 4121.
[64] T. Mitsui, W. B. Westphal, *Phys. Rev.* **1961**, *124*, 1354.